



Development and Testing of Grooved Ceramic Heat Pipes for Intermediate Temperature Systems

Giancarlo D'Orazio*, Andrew van Paridon†, Elaine Petro ‡, and Sadaf Sobhani§
Cornell University, Ithaca, NY, 14853, USA

Traditional low-temperature and high-temperature heat pipes dominate existing thermal control systems, but a significant gap persists in addressing thermal rejection efficiency within the intermediate-temperature range. Ceramics, with their exceptional chemical and thermal stability, offer compatibility with a broad range of working fluids, making them uniquely suited to bridge this gap. This work presents a novel experimental study of additively manufactured (AM) ceramic heat pipes. Grooved alumina envelopes were fabricated and tested with ethanol and Dowtherm A. Mass rate-of-rise experiments were conducted to quantify the effects of silicate glaze coatings on permeability and effective pore radius. Atmospheric heat pipe testing exhibited stable isothermal behavior under a heat flux of up to 5.65 W across the adiabatic section. These findings establish a foundation for leveraging AM ceramic technologies to enhance spacecraft thermal management.

I. Nomenclature

K	=	permeability (m^2)
g	=	gravity (m/s^2)
h	=	rise height (m)
H_{fg}	=	heat of vaporization (kJ/mol)
l_e	=	evaporator length (m)
l_{eff}	=	effective heat pipe length (m)
l_t	=	total heat pipe length (m)
\dot{Q}_b	=	boiling limit (W)
\dot{Q}_c	=	capillary limit (W)
r_{eff}	=	effective pore radius (m)
r_i	=	heat pipe inner radius (m)
r_n	=	nucleation radius (m)
r_s	=	vapor core cross-sectional radius (m)
t	=	time (s)
T_v	=	vapor saturation temperature (K)
X_t	=	wick thickness (m)
X_w	=	wick width (m)
W	=	Lambert W function
ε	=	porosity
μ	=	surface tension ($kg/m \cdot s$)
ρ	=	density (kg/m^3)
σ	=	dynamic viscosity (N/m)
θ	=	orientation angle of capillary

*Graduate Student, Sibley School of Mechanical and Aerospace Engineering, 184 Grumman Hall, 134 Rhodes Dr., Ithaca, NY 14853

†Senior Research Associate, Senior Lecturer, Sibley School of Mechanical and Aerospace Engineering, 130 Upson Hall, 124 Hoy Rd., Ithaca, NY 14853

‡Assistant Professor, Sibley School of Mechanical and Aerospace Engineering, 130 Upson Hall, 124 Hoy Rd., Ithaca, NY 14853, AIAA Member

§Assistant Professor, Sibley School of Mechanical and Aerospace Engineering, 130 Upson Hall, 124 Hoy Rd., Ithaca, NY 14853, AIAA Member

II. Introduction

Long-duration crewed spaceflight to Mars, a central objective of NASA's Artemis program, presents significant engineering challenges, particularly in developing efficient propulsion and thermal management systems. Nuclear Electric Propulsion (NEP) has emerged as a promising solution, providing high specific impulse for interplanetary transit while generating sufficient energy to power propulsion systems, scientific instruments, and life support [1–3]. These systems typically operate at high exit temperatures, ranging from 525°C to 1525°C [4], necessitating robust thermal management solutions. Current designs employ a pumped fluid loop with eutectic liquids, such as sodium-potassium (NaK), to transfer heat to heat pipes, which then reject waste heat through large radiators [5]. Heat pipes can be broadly classified based on operating temperature as low (-70-270°C), intermediate (300-600°C), or high (> 600°C)[6, 7]. The high exit temperatures of NEP reactors preclude the use of most low-temperature working fluids, making intermediate-temperature heat pipes a critical area of development. Intermediate-temperature designs can interface with NaK loops while efficiently rejecting waste heat, addressing a significant gap in current thermal management systems.

Halide-based working fluids have been explored for this temperature range, with some systems operating reliably for years [8–10]. Despite their promise, these fluids are limited by low terrestrial heat rejection capabilities and their reactive nature, which restricts compatibility to specific materials. Examples of halide-based working fluids include aluminum bromide (AlBr_3), aluminum chloride (AlCl_3), antimony tribromide (SbBr_3), iron chloride (FeCl_3), and Dowtherm A (a mixture of diphenyl oxide ($\text{C}_{12}\text{H}_{10}\text{O}$) and biphenyl ($\text{C}_{12}\text{H}_{10}$)). Recent advancements have shown good material compatibility between these fluids and aluminum nitride (AlN) ceramics, offering new opportunities for improved performance in this critical temperature range [11].

Ceramics are uniquely suited for these applications due to their high resistance to reactive chemicals, such as mineral acids and strong bases [12], and their exceptional heat tolerance [13]. Historically, conventionally manufactured ceramics have been used in high-temperature heat exchanger and heat pipe designs to increase conversion efficiency [14, 15]. The advent of ceramic additive manufacturing (AM) has enabled more complex designs with intricate internal structures and tailored thermal properties [16]. Sixel et al. demonstrated the potential of AM ceramic systems for heat rejection by fabricating alumina heat exchangers[17, 18] and subsequently investigated the production of a constant conductance heat pipe via the testing of a sintered heat pipe evaporator[19, 20]. However, the fabrication of heat pipes entirely from ceramics using purely AM techniques remains underexplored. Recent work by Agrawal et al. has advanced this field by producing oscillating heat pipes via robocasting, further demonstrating the potential of AM ceramics for thermal management systems [21].

The recent advancements in AM have not only expanded the design possibilities for heat pipes but also necessitated precise characterization of their fluid transport properties to ensure optimal performance. A key method for such characterization is rate-of-rise testing, which provides critical insights into parameters like permeability (K) and effective pore radius (r_{eff}), wherein a section of the heat pipe wick or grooves are submerged in a working fluid of interest. Commonly, a rising fluid front is captured optically and the rise rate against gravity used to determine K and r_{eff} [22, 23]. This can be calculated as:

$$\frac{dh}{dt} = \frac{1}{h} \frac{K}{\varepsilon \mu} \left(\frac{2\sigma \cos \theta}{r_{\text{eff}}} - \rho g h \right) \quad (1)$$

Where the rate-of-rise is a function of the rise height (h), permeability (K), porosity (ε), surface tension (μ), dynamic viscosity (σ), the angle between the gravity vector and the capillary structure (θ), the effective pore radius (r_{eff}), working fluid density (ρ), and gravity (g). Prior work by Sixel et al. examined the fluid transport properties of alumina heat pipes with sintered wicks using this method [17, 18].

An alternate approach involves measuring the mass rate-of-rise, where the mass change over time (m-t) is recorded using a balance as the heat pipe or wick section is inserted into the working fluid of interest [24–26]. The corresponding rate of mass change is fitted with a Lambert W function:

$$m(t) = \frac{A}{B} \left(1 + W \left(-\exp \left(-1 - \frac{B^2 t}{A} \right) \right) \right) + C t^{\frac{1}{3}} \quad (2)$$

$$A = \frac{2\sigma K \varepsilon (X_t X_w)^2}{\mu r_{\text{eff}}} \quad (3)$$

$$B = \frac{K g X_t X_w \rho^2}{\mu} \quad (4)$$

where A and B are functions of ε , X_t , X_w , r_{eff} , and K which are the wick porosity, thickness, width, effective pore radius, and permeability, respectively and σ , μ , and ρ are the dynamic viscosity, surface tension, and density of the working fluid, g is gravity and C accounts for the secondary wicking effects of the meniscus at the interface of the groove corners. This method offers several practical advantages over traditional optical measurements. Most notably, it does not require a clear line of sight to the entire wick structure, enabling the testing of fully enclosed heat pipe sections. Furthermore, it eliminates the need for post-processing optical data to differentiate between the working fluid front and the wick material, which is a particularly challenging task when using transparent fluids such as water or ethanol.

The experimental values derived from mass rate-of-rise testing provide critical inputs for estimating performance limits of the heat pipe. Work by Nemec et al. describes a one-dimensional model to calculate the capillary, boiling, viscous, sonic, and entrainment limits [27]. Among the most critical, the capillary limit (\dot{Q}_c), dominates the ceramic heat pipe performance from startup to the middle of its operating temperature range, expressed as:

$$\dot{Q}_c = \frac{\rho_l \sigma H_{fg}}{\mu_l} \frac{KA_w}{l_{eff}} \left(\frac{2}{r_{eff}} - \frac{\rho_l g l_t}{\sigma} \cos(\theta) \right) \quad (5)$$

The capillary limit is a function of the working fluid liquid density and viscosity, heat of vaporization (H_{fg}), surface tension of the liquid working fluid, permeability, wick area (A_w), effective (l_{eff}) and total (l_t) heat pipe length, effective pore radius, gravity, and the angle at which the heat pipe is oriented. At the highest temperatures, the boiling limit typically dominates, with the boiling limit (\dot{Q}_b) expressed as:

$$\dot{Q}_b = \frac{4\pi(l_e)k_{eff}\sigma T_v}{H_{fg}\rho_l \ln(r_s/r_i)} \left(\frac{1}{r_n} - \frac{1}{r_{eff}} \right) \quad (6)$$

The boiling limit is a function of the evaporator length (l_e), radii of the vapor core (r_s), inner heat pipe (r_i), and of nucleation (r_n), and finally the vapor saturation temperature (T_v). Both limits require accurate measurements of permeability and effective pore radius, which are obtained from the experimental data. These inputs allow for a detailed assessment of the heat pipe's performance across its operating range.

This work leverages AM ceramics to develop constant conductance heat pipes for use in intermediate-temperature systems, targeting 225-325°C. While AlN ceramic has been identified as an ideal candidate for the envelope material due to its excellent mechanical and thermal properties [11], alumina is utilized in this study as a stand-in ceramic material to determine the optimal groove geometry. This is largely due to the comparative ease of printing and thermally processing of alumina, and its mechanical similarity to AlN. To evaluate the performance of ceramic heat pipes, mass rate-of-rise testing is employed to characterize critical fluid transport properties such as permeability and effective pore radius. The derived permeability and pore radius values are then integrated into heat pipe models to project key operating limits, such as capillary and boiling limits, which inform future heat pipe designs and optimization.

III. Methodology

A. Additive manufacturing and material processing

Heat pipes were fabricated using an Admatec Adamaflex 130 digital light processing (DLP) 3D printer, which allows for the production of high-resolution parts with a minimum feature size of 50 μm and layer heights ranging from 10 to 50 μm . Alumina was chosen as the material for this study due to its higher build rate (5 mm/hr compared to 2 mm/hr for AlN) and less restrictive thermal processing requirements. While alumina has a lower thermal conductivity than AlN, it exhibits similar dimensional accuracy and wetting behavior, making it a suitable stand-in material for initial prototyping. Furthermore, AlN is prone to hydrolysis in humid environments, whereas alumina is more stable under atmospheric conditions, making it more appropriate for bench testing in this work.

Alumina parts were printed with a 30 μm layer height and exposure power of approximately 64 mJ/cm², scaled geometrically by a factor of 1.3 to accommodate for shrinkage during sintering. Heat pipes were printed horizontally, with the width of the heat pipe along that of the print direction. This meant that the heat pipes required support for printing but greatly reduced print time, approximately 3 hours for this print orientation compared to 17 hours for printing in the direction of the heat pipe's length. After printing, the heat pipes had support material removed and were thoroughly cleaned to ensure fully cleared grooves. Parts were subsequently soaked in 40°C water for 24 hours to facilitate removal of some of the water soluble resin and then dried for a minimum of 24 hours. Finally, the components were thermally debound and sintered according to Admatec's recommended debind and sintering protocols, a full discussion of which is well described by Lam et al.[28].

B. Heat pipe design and glazing

In all tests, a 20-tooth groove design was used, with a wick thickness of approximately 0.8 mm as sintered, and inner diameter of 7 mm, and overall length of 65 mm and a wick porosity of 51.1%. In order to facilitate printing in the horizontal direction, internal rings were included to support the groove sections during the print. It is planned to substitute the rings with a conformal printed screen, thus improving both permeability while acting as a support structure during printing. Due to the complex nature of such a hybrid design, the groove-only structure was pursued here, as it serves as a valuable reference point. The groove design utilized in these heat pipes is intended to be easily tailored and adjustable, such that it can be altered to produce optimal thermal transfer for a specific working fluid, shown in Figure 1. Combined with the AM process, it is possible to rapidly prototype heat pipe designs tailored to specific working fluids and heat flux. Proof-of-concept designs are manufactured such that they are compatible with conventional 3/8" Swagelok fittings facilitating charging, degassing, and bench testing without dedicated fixtures for each heat pipe design.

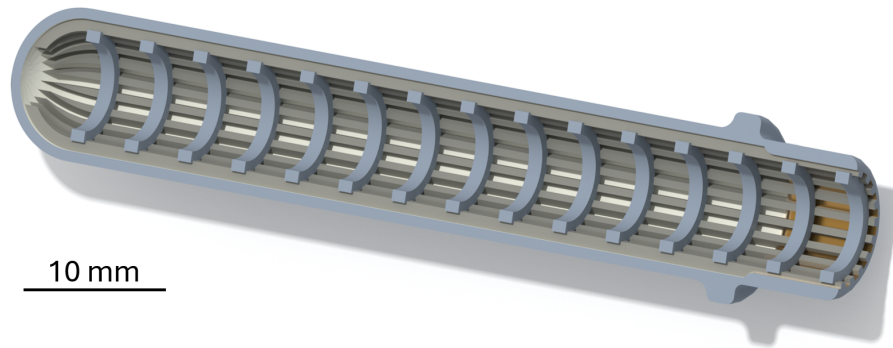


Fig. 1 Section view of the CAD model used to print heat pipes in this work.

In order to test both fluid transport performance and hermeticity of the designs, 65 mm-long sintered heat pipes were glazed with a commercial silicate glaze (Sax True Flow Gloss Glaze). The samples were first coated in a polyvinyl alcohol-water solution to promote adhesion of the liquid glaze, and dried. After this drying period, the glaze was applied with a syringe to evenly coat the area of interest (either the exterior or interior of the heat pipe) and then dried completely for 48 hours before firing to 1250°C (Cone 6) to vitrify the coating. A control unglazed sample was used to ensure that the additional firing did not impact part geometry and ceramic grain size. After glazing, the coating was characterized via scanning electron microscopy (Zeiss Ultra SEM) to confirm coating conformality. Hermeticity testing was conducted with the heat pipes mounted in a Swagelok fitting and vacuum applied until near-zero pressure was achieved. After a period of twenty-four hours, the glazed heat pipes were retested to ensure vacuum was maintained.

C. Rate-of-rise experimentation

Mass rate-of-rise testing employed the m-t method, in which the heat pipe is suspended on a linear stage above Dowtherm A and gradually lowered until the heat pipe's wick or grooves just make contact with the fluid meniscus. The fluid is placed on a balance (Torbay Scales AGZN 220, linearity +/- 0.0002 g, repeatability +/- 0.0001 g), with the mass logged every 0.25 seconds. Compensation for the mass of the meniscus in contact with the heat pipe was measured and corrected before data processing. This data is then fit to using the nonlinear, least-squares *lsqcurvefit* fitting function in Matlab to derive permeability and effective pore radius as outlined by Elkholly et al. [25, 26] and in Equation 2. The fitted coefficients in Equations 3 and 4 are used to derive the permeability and effective pore radius with the known working fluid and heat pipe properties.

D. Heat pipe test setup

An externally glazed alumina heat pipe was tested with ethanol as the working fluid under atmospheric conditions, subjected to a constant heat flux of up to 5.65 W. Ethanol was selected for its widespread use in heat pipe testing and excellent wetting of the alumina envelope material. The heat pipe was mounted to a Swagelok fitting and gate valve, wherein the sample was filled with 375 μ L of ethanol, evacuated of air, and mounted with the evaporator raised approximately one degree above horizontal to prevent thermosiphon effects. A 16-gauge nichrome wire was wrapped

around the evaporator and bonded to the envelope with boron nitride thermal paste (Slice Engineering) and subsequently insulated with alumina wool. This wire was heated with a constant current power supply with the current ramped from 3 to 5 A for initial warm-up and maintained at 5 A and 1.13 V during testing. The condenser section was actively cooled with a fitting brazed to a chilled water loop and insulated with conformal polydimethylsiloxane (Sylgard 184). The fluid loop was maintained at a setpoint of 18 °C and the input and output temperature of the water measured for the duration of the experiment. In order to determine isothermal operation, the adiabatic sections was fitted with three type K thermocouples at 10 mm intervals from the condenser, and the heat rejection measured by the aforementioned chilled fluid loop, shown in Figure 2. Additionally, an infrared thermal camera (FLIR One) was used to monitor operation and highlight temperature gradients along the heat pipe's length.

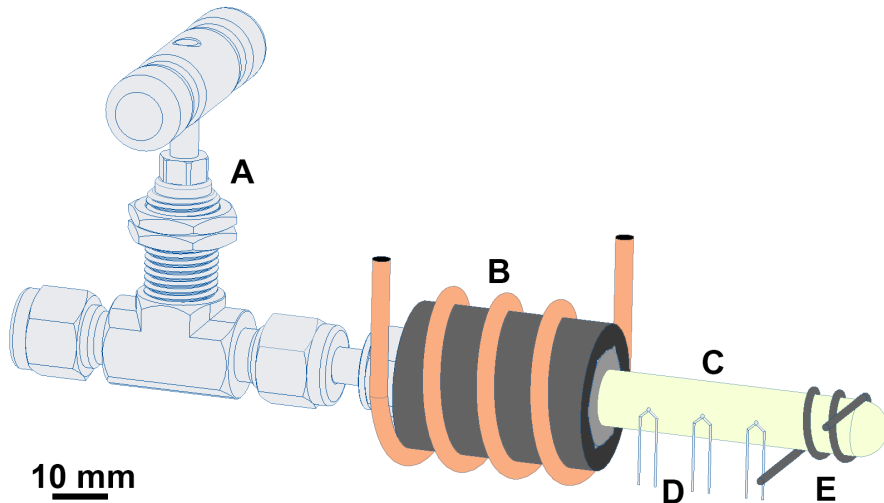


Fig. 2 Schematic of the heat pipe thermal testing apparatus. A) Gate valve for filling. B) Pumped fluid loop on heat pipe condenser. C) Heat pipe mounted in fittings. D) Thermocouples, spaced 10 mm from the condenser. E) Nichrome heater.

IV. Results

A. Heat pipe manufacturing and glazing

All tested heat pipes exhibited slight warping along the print direction after sintering. However, this did not affect the repeatability or reliability of the mass rate-of-rise testing, which was consistent across all printed samples. The parts experienced a shrinkage of approximately 30%, consistent with expectations for alumina sintering using the selected printing system, and this was accounted for by applying a scaling factor of 1.3 during the printing process.

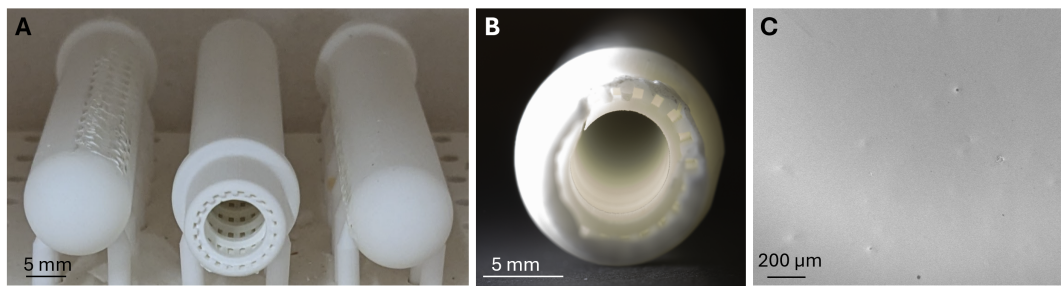


Fig. 3 A) As-printed heat pipes in the debinding furnace and B) A cut section of a sintered heat pipe illustrating the groove profile C) SEM of the Sax glaze on an aluminum nitride sheet, illustrative of glaze conformality.

Visual inspection and Scanning Electron Microscopy (SEM) analysis of the glaze confirmed that the coating was highly conformal and largely defect-free, with no evidence of crazing, as shown in Figure 3. Additionally, no crystalline structures were observed on the surface, indicating that the silicate glaze had fully encapsulated the underlying ceramic in the sampled regions. Vacuum testing further validated the quality of the glazing process, with negligible pressure drop observed over a 24-hour period. This confirmed the hermeticity of the glazed heat pipes, with any vacuum loss attributed primarily to the seal quality of the Swagelok fittings rather than the heat pipe itself.

B. Rate-of-rise results

Figure 4 illustrates the steady state rise height with deionized water and a water soluble dye in partial heat pipe sections. Tested only for illustrative purposes, these sections demonstrate visually the considerably secondary wicking effects which are seen in the externally glazed samples but not present in the internally glazed samples. The internally glazed sample was tested again in the horizontal position which confirmed that pores were not blocked in the region between the support rings and the grooves.

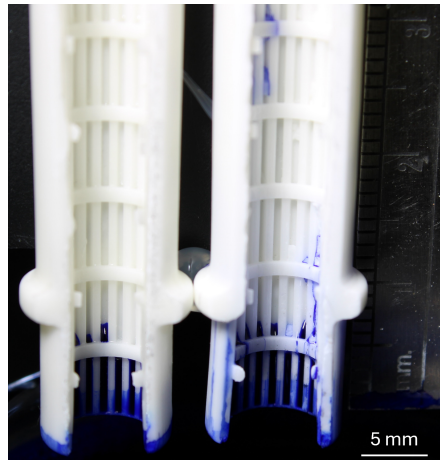


Fig. 4 Steady-state wicking of water in alumina heat pipes, internally glazed (left) and unglazed (right).

Total wick uptake of Dowtherm A was between 0.04 and 0.06 g in all experiments, after correcting for the meniscus mass. Figure 5 illustrates the mass rate-of-rise with Dowtherm A, comparing unglazed, externally glazed and internally glazed samples. The resulting fitted parameters in Equation 2, and consequent permeability and effective pore radius are presented in Table 1.

The sample rate of the balance introduced limitations in capturing data at the start of the experiment, where the fluid rise rate is highest, leading to under-fitting in this initial phase. Modifications to the experimental setup are planned, increasing sample rate by approximately 25 times the current rate. Notable in all mass rate-of-rise experiments was a small, but distinct jump in mass approximately 3.25 seconds into the experimental run, compared to the steady rise before and after, illustrated in Figure 5. This is likely attributed to the working fluid encountering the changes in the internal heat pipe geometry, as the initial support ring is approximately 1 mm from the end of the heat pipe follow by a second support ring 4 mm beyond that, and a corresponding increase in the wick depth.

Permeability varied significantly among the samples, with the unglazed sample exhibiting substantially higher permeability compared to both the externally and internally glazed variants. This trend suggests that permeability is greatest in samples with unglazed internal structures (i.e., as-sintered alumina). This observation may be attributed to secondary effects, such as liquid absorption into the ceramic material, which is more pronounced in unglazed samples with larger effective surface areas in contact with the working fluid. The effective pore radius was similar for the unglazed and internally glazed samples, while the externally glazed sample consistently exhibited a larger value. The cause of this discrepancy is not immediately evident and highlights the need for further investigation. Additional analysis, including destructive testing of the internal pore structure, could provide valuable insights into these observations and inform future design improvements.

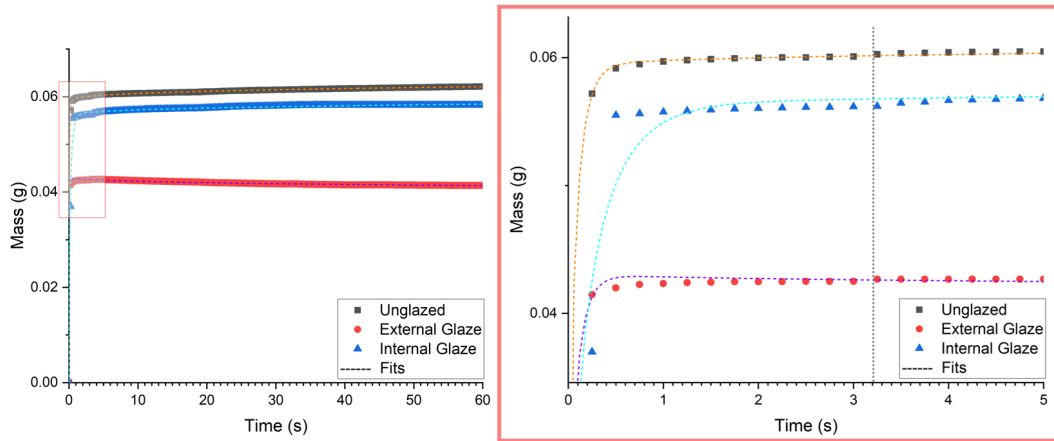


Fig. 5 Mass rate-of-rise results with Dowtherm A comparing three surface coatings (left) and highlighted region of the first 5 seconds of mass uptake (right). A subtle shift in rate-of-rise occurs at approximately 3.25 s into testing.

Table 1 Mass rate-of-rise fitting coefficients and derived permeability and effective pore radius for alumina heat pipes with Dowtherm A.

Surface	A (kg^2/s)	B (kg/s)	C (kg/s^3)	K (m^2)	$r_{\text{eff}} (\text{m})$
Unglazed	3.16E-08	5.35E-04	8.03E-06	10.1E-9	1.42E-03
External Glaze	1.69E-08	3.89E-04	-5.21E-06	7.39E-9	1.93E-03
Internal Glaze	8.14E-08	1.46E-04	0.688E-06	2.77E-9	1.50E-03

C. Heat pipe testing results

The permeability and effective pore radius derived from the rate-of-rise tests were used to compute the expected capillary and boiling limits, and thus set bounds for the maximum operating temperature in atmospheric thermal testing of an ethanol heat pipe. Figure 6 illustrates that the capillary limit is dominant until approximately 137 °C at a power of 13.4 W. Therefore, testing was conducted such that the maximum heat flux was fully within the bounds of these calculated limits. Externally glazed heat pipe was selected, owing to the higher permeability compared to the internally glazed sample. The unglazed sample was not considered due to its lack of hermeticity. Various charge loads were trialed ranging from 250-1000 μL , and in testing a 375 μL volume of ethanol performed consistently at heat fluxes up to 5.65 W. In testing, a notable failure occurred approximately 53 minutes into operation, 8 minutes after ramping to 5.65 W. Temperature at the evaporator spiked sharply from the 68.12 ± 0.26 °C steady state temperature, rising to above 95 °C before the experiment was shut down. During this time, the temperature gradient between the three thermocouples jumped from an average of 0.1°C/mm to 0.6°C/mm and increasing at shutdown. Just before this jump, thermal imaging agrees with the logged thermocouple data, with a minor temperature gradient across the entire adiabatic section, shown in Figure 7. After shutdown, it was confirmed that the heat pipe maintained vacuum and was therefore unlikely to be a root cause of the failure. It is believed that the length of steel fittings beyond the condenser section is a contributor to this failure, as vapor may condense in the fittings and cannot be transported via the wick back to the evaporator. A modification to the mount has been designed to remedy this failure mode. Table 2 highlights the average operating

Table 2 Externally Glazed Heat Pipe Steady State Operating Temperatures

Power In (W)	Condenser out (°C)	10 mm (°C)	20 mm (°C)	30 mm (°C)	Evaporator (°C)	Thermal Gradient (°C/mm)
3.68	17.53 ± 0.86	26.55 ± 0.36	27.06 ± 0.33	28.17 ± 0.22	53.49 ± 0.22	0.08
5.65	18.32 ± 0.14	28.34 ± 0.34	28.90 ± 0.40	30.53 ± 0.33	68.12 ± 0.26	0.11

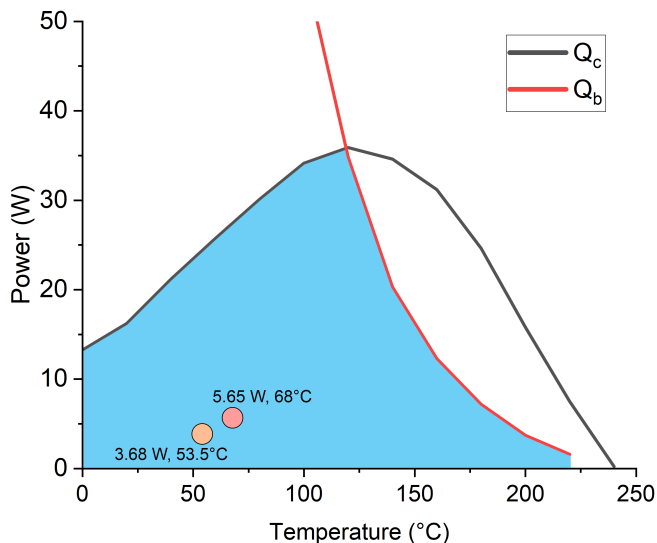


Fig. 6 Calculated capillary (Q_c) and boiling (Q_b) limits for the externally glazed alumina heat pipe using data derived from mass rate-of-rise testing. The effective operating regime is highlighted in blue. The two tested thermal conditions are indicated on the plot.

temperatures in the 3.68 and 5.65 W operating regimes, with the deviation for the duration of steady state operation.

V. Summary and conclusions

Grooved ceramic alumina heat pipes were fabricated using digital light processing (DLP) additive manufacturing, thermally processed, and tested for their fluid transport and thermal performance. Silicate glaze coatings were applied to evaluate their impact on permeability and fluid transport properties. Results showed that internal glaze coatings reduced permeability compared to external coatings, likely due to surface modifications that hinder fluid absorption. Thermal testing demonstrated stable operation of an externally glazed alumina heat pipe charged with 375 μL of ethanol under heat fluxes up to 5.65 W. A minimal temperature gradient across the adiabatic section confirmed effective heat pipe operation. Future efforts will focus on transitioning to high-conductivity ceramics, optimizing hybrid groove designs to enhance fluid transport, and integrating these heat pipes into advanced thermal management systems. Testing with a wider range of working fluids is planned, notably with halides which typically require careful pairing with metal envelope materials. These developments position ceramic heat pipes as a transformative technology for spacecraft and terrestrial applications, bridging the gap between low- and high-temperature regimes and unlocking new possibilities in efficient thermal control.

Acknowledgments

This work was supported by the NASA Early Stage Innovations grant (grant number 80NSSC23K0236). The authors also acknowledge the use of facilities and instrumentation funded by the National Science Foundation through the Cornell University Materials Research Science and Engineering Center (DMR-1719875). Special thanks are extended to Mirian Vargas for their support on this project and to William Sixel for their insightful discussions.

References

- [1] Pawlik, E. V., and Phillips, W. M., "A Nuclear Electric Propulsion Vehicle for Planetary Exploration," *Journal of Spacecraft and Rockets*, Vol. 14, No. 9, 1977, pp. 518–525. <https://doi.org/10.2514/3.57233>, URL <https://doi.org/10.2514/3.57233>, publisher: American Institute of Aeronautics and Astronautics _eprint: <https://doi.org/10.2514/3.57233>.

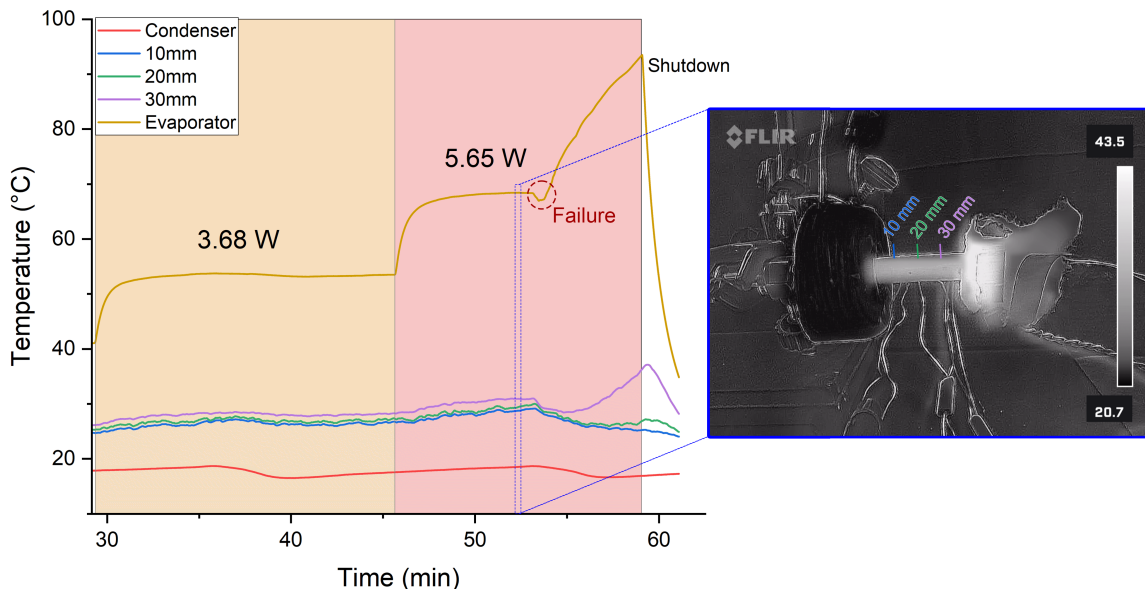


Fig. 7 (Left) Thermocouple measurements across two thermal regimes, 3.68 W and 5.65 W, illustrating isothermal behavior of the adiabatic section until failure and shutdown. Thermocouple measurements are taken at the condenser, in 10 mm increments from the condenser, and the evaporator. **(Right)** FLIR image illustrating the temperature gradient across the envelope.

- [2] Jones, R. M., and Sauer, C. G., “Nuclear electric propulsion missions,” *Journal of the British Interplanetary Society*, Vol. 37, 1984, pp. 395–400. URL <https://ui.adsabs.harvard.edu/abs/1984JBIS...37..395J>, aDS Bibcode: 1984JBIS...37..395J.
- [3] Miao, X., Zhang, H., Wang, Q., Xia, Y., and Sun, W., “Optimum design of nuclear electric propulsion spacecraft for deep space exploration,” *Energy Reports*, Vol. 8, 2022, pp. 9629–9641. <https://doi.org/10.1016/j.egyr.2022.07.146>, URL <https://www.sciencedirect.com/science/article/pii/S2352484722014123>.
- [4] *Space Nuclear Propulsion for Human Mars Exploration*, National Academies Press, Washington, D.C., 2021. <https://doi.org/10.17226/25977>, URL <https://www.nap.edu/catalog/25977>.
- [5] Machemer, W. S., Duchek, M. E., and Nikitaev, D., “Considerations for Radiator Design in Multi-Megawatt Nuclear Electric Propulsion Applications,” *AIAA SCITECH 2023 Forum*, AIAA SciTech Forum, American Institute of Aeronautics and Astronautics, 2023. <https://doi.org/10.2514/6.2023-0152>, URL <https://arc.aiaa.org/doi/10.2514/6.2023-0152>.
- [6] Jouhara, H., Chauhan, A., Nannou, T., Almahmoud, S., Delpech, B., and Wrobel, L. C., “Heat pipe based systems - Advances and applications,” *Energy*, Vol. 128, 2017, pp. 729–754. <https://doi.org/10.1016/j.energy.2017.04.028>, URL <https://www.sciencedirect.com/science/article/pii/S0360544217305935>.
- [7] Werner, T. C., Yan, Y., Karayannidis, T., Pickert, V., Wrobel, R., and Law, R., “Medium temperature heat pipes – Applications, challenges and future direction,” *Applied Thermal Engineering*, Vol. 236, 2024, p. 121371. <https://doi.org/10.1016/j.applthermaleng.2023.121371>, URL <https://www.sciencedirect.com/science/article/pii/S135943112301400X>.
- [8] Anderson, W., Dussinger, P., Bonner, R., and Sarraf, D., “High Temperature Titanium/Water and Monel/Water Heat Pipes,” *4th International Energy Conversion Engineering Conference and Exhibit (IECEC)*, American Institute of Aeronautics and Astronautics, San Diego, California, 2006. <https://doi.org/10.2514/6.2006-4113>, URL <https://arc.aiaa.org/doi/10.2514/6.2006-4113>.
- [9] Sarraf, D. B., and Anderson, W. G., “Heat Pipes for High Temperature Thermal Management,” American Society of Mechanical Engineers Digital Collection, 2010, pp. 707–714. <https://doi.org/10.1115/IPACK2007-33984>, URL <https://asmedigitalcollection.asme.org/InterPACK/proceedings-abstract/InterPACK2007/42770/707/324319>.
- [10] Anderson, W., G., Tarau, C., and Ellis, D. L., “Intermediate Temperature Heat Pipe Working FLuids,” *Heat Pipes: Design, Applications and Technology*, Nova Science Publishers, 2018, pp. 395–423.

- [11] D'Orazio, G., Sixel, W. R., and Sobhani, S., "Additive Manufacturing and Working Fluid Characterization of Ceramic Heat Pipes," *AIAA SCITECH 2024 Forum*, American Institute of Aeronautics and Astronautics, Orlando, FL, 2024. <https://doi.org/10.2514/6.2024-1792>, URL <https://arc.aiaa.org/doi/10.2514/6.2024-1792>.
- [12] Krasnyi, B. L., Tarasovskii, V. P., Rakhmanova, E. V., and Bondar', V. V., "Chemical Resistance of Ceramic Materials in Acids and Alkalies," *Glass and Ceramics*, Vol. 61, No. 9, 2004, pp. 337–339. <https://doi.org/10.1023/B:GLAC.0000048706.05368.71>, URL <https://doi.org/10.1023/B:GLAC.0000048706.05368.71>.
- [13] Justin, J., and Jankowiak, A., "Ultra High Temperature Ceramics : Densification, Properties and Thermal Stability." *Aerospace Lab*, , No. 3, 2011, pp. p. 1–11. URL <https://hal.science/hal-01183657>, publisher: Alain Appriou.
- [14] Ranken, W. A., "Ceramic heat pipe heat exchangers," Tech. Rep. LA-6514-MS, Los Alamos National Lab. (LANL), Los Alamos, NM (United States), Sep. 1976. <https://doi.org/10.2172/7135553>, URL <https://www.osti.gov/biblio/7135553>.
- [15] Strumpf, H. J., "Ceramic heat pipes for high-temperature heat recovery," *Journal of Heat Recovery Systems*, Vol. 2, No. 2, 1982, pp. 189–199. [https://doi.org/10.1016/0198-7593\(82\)90046-7](https://doi.org/10.1016/0198-7593(82)90046-7), URL <https://www.sciencedirect.com/science/article/pii/0198759382900467>.
- [16] Scheithauer, U., Schwarzer, E., Moritz, T., and Michaelis, A., "Additive Manufacturing of Ceramic Heat Exchanger: Opportunities and Limits of the Lithography-Based Ceramic Manufacturing (LCM)," *Journal of Materials Engineering and Performance*, Vol. 27, No. 1, 2018, pp. 14–20. <https://doi.org/10.1007/s11665-017-2843-z>, URL <https://link.springer.com/article/10.1007/s11665-017-2843-z>, company: Springer Distributor: Springer Institution: Springer Label: Springer Number: 1 Publisher: Springer US.
- [17] Sixel, W., Liu, M., Nellis, G., and Sarlioglu, B., "Ceramic 3D Printed Direct Winding Heat Exchangers for Improving Electric Machine Thermal Management," *2019 IEEE Energy Conversion Congress and Exposition (ECCE)*, 2019, pp. 769–776. <https://doi.org/10.1109/ECCE.2019.8913234>, iSSN: 2329-3748.
- [18] Sixel, W., Liu, M., Nellis, G., and Sarlioglu, B., "Ceramic 3-D Printed Direct Winding Heat Exchangers for Thermal Management of Concentrated Winding Electric Machines," *IEEE Transactions on Industry Applications*, Vol. 57, No. 6, 2021, pp. 5829–5840. <https://doi.org/10.1109/TIA.2021.3104273>, conference Name: IEEE Transactions on Industry Applications.
- [19] Sixel, W., Kaviani, M., and Leary, A., "Ceramic Heat Pipe for Thermal Management of a High-Frequency Inductor," *AIAA Propulsion and Energy 2021 Forum*, AIAA Propulsion and Energy Forum, American Institute of Aeronautics and Astronautics, 2021. <https://doi.org/10.2514/6.2021-3335>, URL <https://arc.aiaa.org/doi/10.2514/6.2021-3335>.
- [20] Sixel, W., Kaviani, M., Hwang, G., and Egbo, M. K., "Experimental Demonstration and Characterization of a Ceramic Sintered Wick Heat Pipe Evaporator," *AIAA AVIATION 2023 Forum*, AIAA AVIATION Forum, American Institute of Aeronautics and Astronautics, 2023. <https://doi.org/10.2514/6.2023-3878>, URL <https://arc.aiaa.org/doi/10.2514/6.2023-3878>.
- [21] Agrawal, P., Ahmadi, B., Cesarano, J., and Bigham, S., "3D-printed Ceramic Oscillating Heat Pipes for Improved Electronic Thermal Management," *2024 23rd IEEE Intersociety Conference on Thermal and Thermo-mechanical Phenomena in Electronic Systems (ITherm)*, 2024, pp. 1–5. <https://doi.org/10.1109/ITherm55375.2024.10709538>, URL https://ieeexplore.ieee.org/abstract/document/10709538?casa_token=6n_tT9m7vN0AAAAAA:e3NkfH7t7hQiWj0Hth9f5lGKm76VxghH9Z8ORfydCmErb_8HO6IVbTJ8YtS6VnKfMK5swUx1nw, iSSN: 2694-2135.
- [22] Adkins, D. R., and Dykhuizen, R. C., "Procedures for measuring the properties of heat-pipe wick materials," Tech. Rep. SAND-92-2347C; CONF-930804-14, Sandia National Labs., Albuquerque, NM (United States), Jul. 1993. URL <https://www.osti.gov/biblio/10177198>.
- [23] Reed, C. M., and Wilson, N., "The fundamentals of absorbency of fibres, textile structures and polymers. I. The rate of rise of a liquid in glass capillaries," *Journal of Physics D: Applied Physics*, Vol. 26, No. 9, 1993, p. 1378. <https://doi.org/10.1088/0022-3727/26/9/006>, URL <https://dx.doi.org/10.1088/0022-3727/26/9/006>.
- [24] Ponomarenko, A., Quéré, D., and Clanet, C., "A universal law for capillary rise in corners," *Journal of Fluid Mechanics*, Vol. 666, 2011, pp. 146–154. <https://doi.org/10.1017/S0022112010005276>, URL <https://www.cambridge.org/core/journals/journal-of-fluid-mechanics/article/universal-law-for-capillary-rise-in-corners/D70D4365220A10A140B6C63D16D3A565>.
- [25] Elkholy, A., Bardoel, M., Durfee, J., and Kempers, R., "A mass rate-of-rise model for additively manufactured wick structures," *International Communications in Heat and Mass Transfer*, Vol. 146, 2023, p. 106934. <https://doi.org/10.1016/j.icheatmasstransfer.2023.106934>, URL <https://www.sciencedirect.com/science/article/pii/S0735193323003238>.

- [26] Elkholly, A., Durfee, J., Mooney, J. P., Robinson, A. J., and Kempers, R., “A rate-of-rise facility for measuring properties of wick structures,” *Measurement Science and Technology*, Vol. 34, No. 4, 2023, p. 045301. <https://doi.org/10.1088/1361-6501/acad1c>, URL <https://dx.doi.org/10.1088/1361-6501/acad1c>, publisher: IOP Publishing.
- [27] Nemeč, P., Čaja, A., and Malcho, M., “Mathematical model for heat transfer limitations of heat pipe,” *Mathematical and Computer Modelling*, Vol. 57, No. 1, 2013, pp. 126–136. <https://doi.org/10.1016/j.mcm.2011.06.047>, URL <https://www.sciencedirect.com/science/article/pii/S0895717711003888>.
- [28] Lam, B. C., Kassner, C. T., Kemp, J. W., Leicht, B. T., Bohan, B. T., and Rueschhoff, L. M., “Delamination mitigation in additively manufactured Al₂O₃ via enhanced thermal postprocessing,” *International Journal of Applied Ceramic Technology*, Vol. 21, No. 2, 2024, pp. 675–685. <https://doi.org/10.1111/ijac.14572>, URL <https://onlinelibrary-wiley-com.proxy.library.cornell.edu/doi/abs/10.1111/ijac.14572>, _eprint: <https://ceramics.onlinelibrary.wiley.com/doi/pdf/10.1111/ijac.14572>.